Ultrahigh Carrier Mobility Achieved in Photoresponsive Hybrid Perovskite Films via Coupling with Single-Walled Carbon Nanotubes

Item Type	Article
Authors	Li, Feng; Wang, Hong; Kufer, Dominik; Liang, Liangliang; Yu, Weili; Alarousu, Erkki; Ma, Chun; Li, Yangyang; Liu, Zhixiong; Liu, Changxu; Wei, Nini; Wang, Fei; Chen, Lang; Mohammed, Omar F.; Fratalocchi, Andrea; Liu, Xiaogang; Konstantatos, Gerasimos; Wu, Tao
Citation	Li F, Wang H, Kufer D, Liang L, Yu W, et al. (2017) Ultrahigh Carrier Mobility Achieved in Photoresponsive Hybrid Perovskite Films via Coupling with Single-Walled Carbon Nanotubes. Advanced Materials: 1602432. Available: http://dx.doi.org/10.1002/adma.201602432.
Eprint version	Post-print
DOI	10.1002/adma.201602432
Publisher	Wiley
Journal	Advanced Materials
Rights	This is the peer reviewed version of the following article: Ultrahigh Carrier Mobility Achieved in Photoresponsive Hybrid Perovskite Films via Coupling with Single-Walled Carbon Nanotubes, which has been published in final form at http://doi.org/10.1002/adma.201602432. This article may be used for non-commercial purposes in accordance With Wiley Terms and Conditions for self-archiving.

Ultrahigh Carrier Mobility Achieved in Photo-responsive Hybrid Perovskite Films via Coupling with Single-Walled Carbon Nanotubes

Feng Li, Hong Wang, Dominik Kufer, Liangliang Liang, Weili Yu, Erkki Alarousu, Chun Ma, Yangyang Li, Zhixiong Liu, Changxu Liu, Nini Wei, Fei Wang, Lang Chen, Omar F. Mohammed, Andrea Fratalocchi, Xiaogang Liu, Gerasimos Konstantatos, and *Tom Wu**

Dr. F. Li,[+] Dr. H. Wang,[+] C. Ma, Y. Li, Z. Liu, Prof. T. Wu
Materials Science and Engineering
King Abdullah University of Science and Technology
Thuwal 23955-6900, Saudi Arabia
E-mail: tao.wu@kaust.edu.sa
D. Kufer, Prof. G. Konstantatos
ICFO- Institut de Ciencies Fotoniques
Mediterranean Technology Park, 08860 Castelldefels, Barcelona, Spain
L. Liang, Prof. X. Liu
Department of Chemistry
National University of Singapore
Singapore 117543, Singapore
Dr. W. Yu, Dr. E. Alarousu, Prof. O. F. Mohammed
Solar and Photovoltaics Engineering Research Center
King Abdullah University of Science and Technology
Thuwal 23955-6900, Saudi Arabia
C. Liu, Prof. A. Fratalocchi
PRIMALIGHT
Faculty of Electrical Engineering
Applied Mathematics and Computational Science
King Abdullah University of Science and Technology
Thuwal 23955-6900, Saudi Arabia
Dr. N. Wei
Core lab
King Abdullah University of Science and Technology
Thuwal 23955-6900, Saudi Arabia
Prof. F. Wang, Prof. L. Chen
Department of Electronic and Electrical Engineering
South University of Science and Technology of China
Shenzhen 518055, P.R. China.
Prof. G. Konstantatos
ICREA-Institució Catalana de Recerca i Estudis Avançats
Passeig Lluís Companys, 23, 08010 Barcelona, Spain

[+]F.L. and H.W. contributed equally to this work.

Methylammonium lead trihalide perovskites (MAPbX$_3$, X: Cl, Br or I) feature fascinating chemical and physical properties, including tunable bandgap, large light absorption coefficient in the UV-Vis spectral region, long carrier diffusion length, and solution processability.[1-5] As such, this class of materials has been intensively exploited for developing optoelectronic devices such as solar cells, light-emitting diodes, photodetectors, and phototransistors.[6-20] Thus far, solution processing is the most widely used technique to synthesize perovskite films due to its low cost and simplicity. Furthermore, a recent transient THz spectroscopy study showed that bi-molecular recombination rates are much lower than the fundamental Langevin limit in such perovskite films, leading to high carrier mobilities.[3] However, solution-processed pristine polycrystalline films still suffer from structural imperfections such as grain boundaries, trapping defects and drifting cations.[21,22] Perovskite single crystals have shown exceptionally good structural and physical properties,[23-25] but their bulk form impedes practical device applications. In order to improve the performance of perovskite-based devices, particularly photodetectors, a few works have been devoted to interfacing perovskite films with other functional materials.[18,26] In fact, such an interface-based approach has been applied to a wide range of optoelectronic devices in achieving optimal performance because of the synergistic effect of individual building blocks.[27-32]

Inspired by the extraordinary physical properties of semiconducting single-walled carbon nanotubes (CNTs),[33-37] particularly their ultrahigh charge carrier mobility, we reasoned that marrying halide perovskites with CNTs in composite films could be a viable approach toward high-performance optoelectronics. However, CNTs tend to aggregate into bundles due to the strong intra-tube van der Waals attraction, which is a severe obstacle for its integration with other materials through solution processing.[38] Surprisingly, we found that the perovskite precursor in N,N-dimethylformamide (DMF) solution is an excellent stabilizer for the homogeneous dispersion of semiconducting CNTs with a (7,6) chirality. This composite

material combines the light-absorbing characteristics of perovskites with the high-mobility property of semiconducting CNTs.

Our design principle for the $CH_3NH_3PbI_{3-x}Cl_x$/CNTs composites is illustrated in **Figure 1a**. On light illumination, an efficient transfer of the photo-excited holes from the perovskite matrix to semiconducting CNTs is likely to occur, resulting in a significant reduction in charge recombination and hence enhanced carrier transport. The CNTs were characterized by transmission electron microscopy (TEM, Figure S1) and Raman spectroscopy (see Figure S2), and they are approximately 0.5-2 μm in length and 1.2-1.4 nm in diameter. Subsequently, we dispersed the CNTs in a DMF solution of CH_3NH_3I and $PbCl_2$. Intriguingly, a homogeneous, dark dispersion formed and remained stable for more than 24 h without any noticeable precipitation. In contrast, the pristine CNTs quickly precipitated out in DMF solution under identical conditions (see Figure S3). This excellent dispersibility is of significant importance for device fabrication as CNTs usually agglomerate into bundles during preparation because of the intra-tube van der Waals intra-tube interactions. The much-improved dispersion of CNTs in the $CH_3NH_3PbI_{3-x}Cl_x$/DMF solution could be attributed to the strong electrostatic repulsion between CNTs that are attached with charged $CH_3NH_3^+$ units in the perovskite precursor solution.

TEM images of the perovskite/CNT composite film (see Figure S4) further confirmed that crystalline perovskite closely interface with CNTs. Furthermore, the hybrid layer composed of interpenetrating networks of CNTs in $CH_3NH_3PbI_{3-x}Cl_x$ matrix exhibited a uniform and continuous surface, as observed in the scanning electron microscopy (SEM, Figure S5a) experiment. In comparison, the reference $CH_3NH_3PbI_{3-x}Cl_x$ film suffered from poor surface coverage and pinholes (Figure S5b). Furthermore, atomic force microscopy (AFM) image shown in Figure S6a confirms the smooth morphology of the composite film, whereas the pristine perovskite film is rougher with grains up to hundreds of nanometers in size (Figure S6b). The improved morphology of the composite films can be ascribed to the excellent

compatibility of $CH_3NH_3PbI_{3-x}Cl_x$ and CNTs. Finally, the X-ray diffraction (XRD) pattern of the perovskite/SWNTs composite film in Figure S7 revealed that $CH_3NH_3PbI_{3-x}Cl_x$ in the channel layer remains highly crystalline.
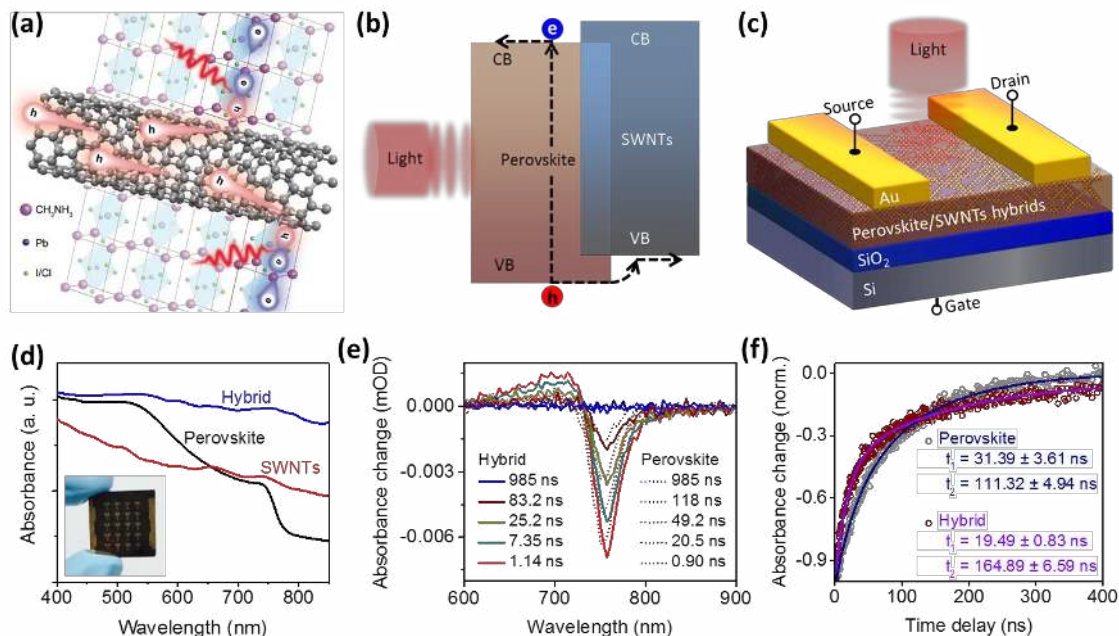

Figure 1. Design and characterizations of the perovskite/CNTs hybrids. (a) Schematic illustrating the mechanism of fast carrier transport in the perovskite/CNTs composites. Photo-generated holes are injected into the CNTs, while electrons are mainly transported by the hybrid perovskite. (b) Energy-level alignment between perovskite and CNTs. CB, conduction band; VB, valence band. (c) Schematic of the perovskite/CNT phototransistor. (d) Absorption spectra of the perovskite/CNT composite, the $CH_3NH_3PbI_{3-x}Cl_x$ and the CNTs samples. (e) Transient absorption spectra of the composite film measured with light excitation at 480 nm. (f) Normalized kinetic traces for ground-state bleach of the perovskite and the composite films probed at 760 nm and 755 nm, respectively.

Besides the structural compatibility, halide perovskite and semiconducting CNTs form a type-II heterojunction, as revealed by a recent photoemission spectroscopy study.[39] As shown in Figure 1b, the valence band (VB) of CNTs aligns well with the VB of $CH_3NH_3PbI_{3-x}Cl_x$, which facilitates the injection of photo-excited holes from perovskite into CNTs. In fact, CNT composites have recently been used as hole transporting materials in

perovskite solar cells.[40] In the hybrid channel, hole-electron pairs are first generated in the hybrid film, and then the holes are injected into CNTs and transported along the CNTs under an applied electric field. The photo-excited electrons predominantly remain and migrate in the perovskite matrix. Importantly, such excited state charge transfer at the CNT/perovskite interface is expected to enhance the transport of both photo-excited electrons and holes via reduced charge recombination.

As a prototypical demonstration of optoelectronic devices, phototransistors, which find a broad range of applications in communication, security, lighting, imaging, and data storage technologies,[41] were fabricated using the perovskite/CNTs hybrid as the active channel. The schematic diagram of our phototransistors is illustrated in Figure 1c. A heavily n-doped Si wafer with a 300-nm SiO_2 surface layer (capacitance C_i: 15 nF cm^{-2}) was employed as the substrate. The perovskites are employed as the light absorber, while CNTs are used to facilitate the transportation of photo-excited carriers. In our devices, the thickness of active films is optimized as 400 nm. It should be noted that a thicker film is likely to result in the screening of gate bias, degrading the device performance.[16]

The wavelength-dependent absorbance of the hybrid perovskite/CNTs thin film is shown in Figure 1d. The optical absorbance of the pure perovskite and pure CNTs layers was also characterized as references. The light absorption in the hybrid film was substantially enhanced in the long-wavelength region as compared to the reference $CH_3NH_3PbI_{3-x}Cl_x$ film. The observed enhancement could be attributed to the strong light absorption of CNTs.[36] The improvement of light absorption in the hybrid active layer is beneficial in improving the photosensitivity and detectivity of the hybrid phototransistor. Overall, the strong and broadband light absorption in the ultraviolet and visible-light regimes underscored the hybrid perovskite/CNTs films as an excellent light absorber, promising for high-performance light-harvesting and optoelectronic applications.

Transient absorption spectroscopy can provide direct information regarding the carrier dynamics and excited-state deactivation pathways.[42] As shown in Figure 1e, sharp negative absorption peaks at around 760 nm and broad positive spectra above the bandgap in both perovskite and composite films were observed, which may be attributed to the ground-state bleach and quasi-equilibrium carrier distribution, respectively. In a recent report, a sub-bandgap transient absorption was observed and explained by the interplay of bandgap renormalization and hot-carrier distribution.[43] More importantly, the ground-state bleach recovery, which mainly reflects the charge recombination, is slower in the composite film compared to the pristine $CH_3NH_3PbI_{3-x}Cl_x$. This is in line with the expected charge separation at the perovskite/CNT interfaces (see Figure 1a). Furthermore, as shown in Figure 1f, The increase in the bulk charge recombination time constant (τ_2) of the composite channel is expected to enhance the performance of such phototransistors.[16,35] The steady-state photoluminescence (PL) was also performed to corroborate the scenario of charge transfer at the perovskite/CNT interface. A strong quenching of the perovskite PL was observed upon the addition of CNTs (see Figure S8), further evidencing the excited state interaction at the perovskite/CNTs interface, in line with previous reports on such composites.[18,26]

We now turn to the electrical properties of the hybrid phototransistor and propose an operating mechanism. To obtain the transfer characteristics (I_{DS}-V_{GS}) of the hybrid phototransistor in dark (**Figure 2a**) and under light illumination (Figure 2b), we swept the backgate voltage V_{GS} while keeping the source–drain bias V_{DS} across the hybrid channel at fixed values. It should be noted that our device, no matter in the dark or under light, shows clear ambipolar behaviors, i.e., I_{DS} increases with V_{GS} on both polarities. In the absence of light (Figure 2a), the source-drain current was found to remain below 10 μA in the measurement range of V_{GS}. In contrast, when the device was illuminated with a white light-emitting diode (LED) at a photoexcitation intensity (E_{light}) of 10 mW cm^{-2}, the channel current reached the level of 10 mA (Figure 2b), indicating a very high photosensitivity.

The field-effect mobility (μ) and threshold voltage (V_{TH}) can be extracted from the linear

regimes of the transfer curves according to:[44]

$$I_{DS} = \frac{W}{L} C_i \mu (V_{GS} - V_{TH}) V_{DS} \qquad (1)$$

where W and L are are the width and length of the channel, respectively, and C_i is the gate

dielectric capacitance per unit area. By fitting the experimental data to equation (1), the field-

effect hole and electron mobilities in the dark were estimated as 0.175 and 0.058 cm^2 V^{-1} s^{-1},

respectively (Figure 2a). More importantly, in the presence of light illumination, the obtained

mobilities of photo-generated holes and electrons are as high as 595.3 and 108.7 cm^2 V^{-1} s^{-1},

respectively (Figure 2b), which are more than two orders of magnitude higher than the values

previously reported for pristine perovskite films (see a comparison in Table S1). The

significant increase in hole/electron mobilities upon illumination with respect to the dark

measurements suggests that the mobility of photo-induced carriers is much higher than that of

intrinsic carriers, which is in line with our previous work on phototransistors with pure

perovskite channels.[16] Furthermore, the ultrahigh room-temperature carrier mobility obtained

here is comparable to the values of high-quality crystalline silicon,[45] which unambiguously

showcases the suitability of the hybrid perovskite/CNTs films for high-mobility

optoelectronic applications.

In line with our previous report,[16] for perovskite phototransistors without CNTs, the field-

effect hole/electron mobilites are only 1.62 × 10^{-4}/1.17 × 10^{-4} cm^2 V^{-1} s^{-1} under the dark

condition and 1.37/0.87 cm^2 V^{-1} s^{-1} under light illumination (Figure S9). It is obvious that the

addition of CNTs significantly improves charge transport in the phototransistor channel. Even

in dark, adding CNTs increased the channel current from the nA to the μA level. This also

indicates that the channel/electrode interfaces are quite transparent in the hybrid devices,

allowing high current to flow through. The high-mobility CNTs embedded in the perovskite

matrix provide fast tracks for carriers to transport with less scattering, which benefits from the good interface and effective charge transfer between perovskites and CNTs.

Generally, various scattering mechanisms, particularly Coulomb scatterings from trapped charges, have a detrimental effect on the mobility of mobile charges in transistor channels.[46] There are several reasons why scatterings in our composite transistor channels are significantly reduced, which accounts for the observed high carrier mobility. First, in the perovskite/CNT composite channel, electrons and holes are separated as a result of type-II interface band alignment,[39] so that the Coulomb scatterings between the photo-carriers are significantly suppressed, which is probably the main factor underlying the observed superior transport. Second, SEM and AFM measurements showed that the hybrid perovskite/CNT film is free from pinholes and much smoother than the pure perovskite film (Figure S5b and Figure S6b). Thus, the deleterious scattering effect from surface roughness will be suppressed. Finally, the high quality of the perovskite/CNT film indicates that charge traps and ionic defects located in the transistor channel are reduced. Charged defects such as methylammonium cations in hybrid perovskites are highly mobile and can drift under the influence of an electrical field. This has been proposed as the origin of notable hysteresis reported for a wide range of perovskite-based optoelectronic devices.[12,16] In contrast, in our hybrid perovskite/CNTs films, the suppressed Coulomb scatterings between the trapped charges and the mobile charges, which is reflected by the ignorable hysteresis in the electrical measurements (Figure 2), lead to conductivity and mobility enhancement.

As shown in Figure 2c,d, the typical output characteristics (that is, the dependence of I_{DS} on V_{DS} at different V_{GS}) of the hybrid phototransistor are ambipolar, which are consistent with the transfer curves. As expected, both the incident light illumination and the gate voltages can substantially modulate the channel transport. Without the gate voltages, the output curves of the hybrid channel, in the absence and presence of light illumination, appear almost symmetric. However, with a high negative V_{GS}, the channel transport exhibits the

characteristics of a diode with good rectification ratios, while a high positive V_{GS} reverses the

rectification of the diode. Furthermore, these data indicate that p-type conduction is slightly

favored, i.e., higher current is consistently achieved with a negative gate bias. As expected,

without any gate bias, the channel transport showed a symmetric behavior without any current
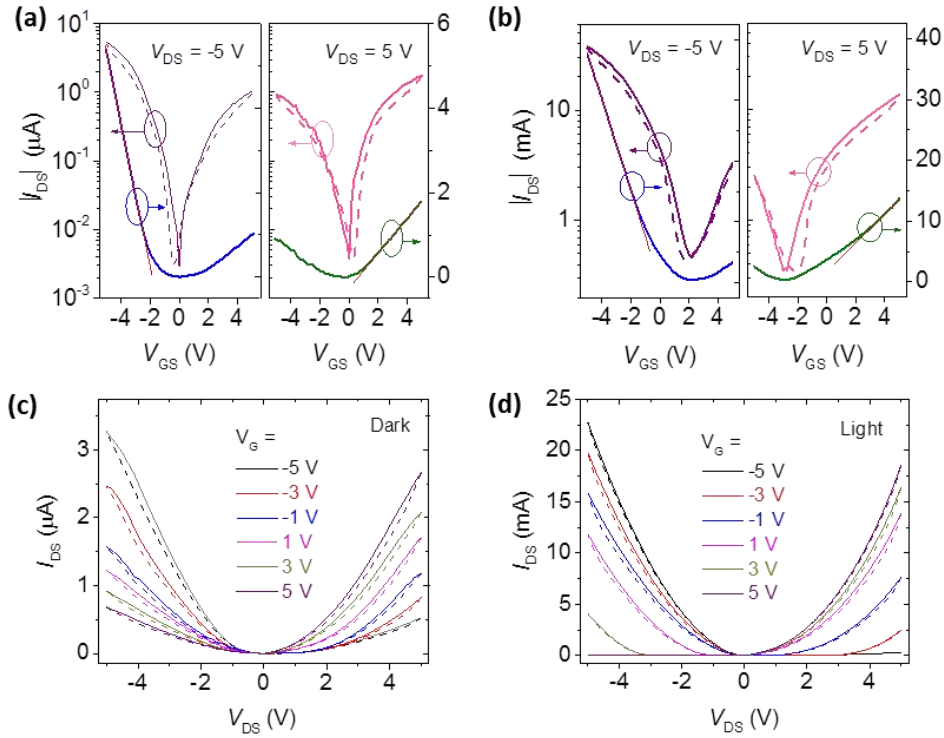
rectification (Figure S10).

Figure 2. Ambipolar transport of the hybrid perovskite/CNTs phototransistor. (a, b) Transfer characteristics (I_{DS}-V_{GS}) of the hybrid perovskite/CNTs phototransistor operating in the absence and presence of light, respectively. (c, d) Output characteristics (I_{DS}-V_{DS}) of the hybrid phototransistor operating in dark and under light illumination, respectively. In (a-d), the solid lines are data taken with voltage scanning from -5 V to + 5 V, while the dashed lines represent the reverse voltage scans.

Photoresponsivity, R, which defines how efficiently the optoelectronic device responds to

an optical signal, is an important figure-of-merit for evaluating the performance of

phototransistors. It is given by: $R = (I_{light}-I_{dark})/E_{light}$, where I_{light} and I_{dark} are the channel

currents under light illumination and in dark, respectively. R as a function of V_{GS} measured on

our phototransistors is shown in **Figure 3a**, with a maximum of approximately 1.17×10^{4} A

W^{-1}. Note that this R value is among the largest values reported for photodetectors.[14,16,18-20,47-50] In contrast, the maximum R of a $CH_3NH_3PbI_{3-x}Cl_x$-based phototransistor is about 13 A W^{-1} (see Figure S11a). The four orders of magnitude enhancement obtained from the hybrid phototransistors indicates the synergic effect of combined halide perovskite and CNTs in the hybrid channel.
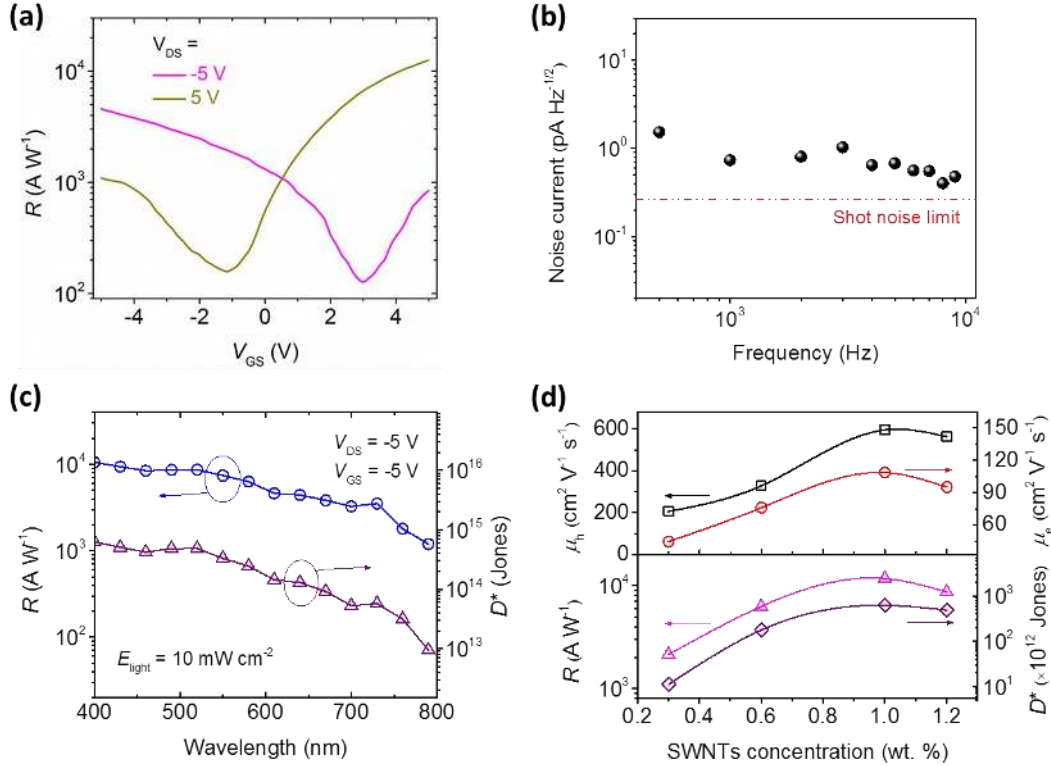

Figure 3. Performance of the hybrid perovskite/CNTs phototransistor. (a) Responsivity (R) of the phototransistor as a function of back-gate voltage. The maximum responsivity reaches approximately 1.17×10^4 A W^{-1}. (b) Noise current of the hybrid phototransistor. Measured noise current of the hybrid perovskite/CNTs phototransistor at different frequencies. The calculated shot noise limit is also plotted for comparison. (c) Responsivity (R) and Detectivity (D^*) of the hybrid phototransistor measured at different wavelengths with the light intensity of 10 mW cm^{-2}. (d) Effect of the CNTs concentration on the performance of the hybrid perovskite/CNTs phototransistor. μ_h, μ_e, R and D^* denote hole mobility, electron mobility, responsivity and detectivity, respectively.

Specific detectivity D^*, which characterizes the ability of the devices to detect the incident light signal is another critical parameter for evaluating the photodetector's performance. The

noise current is the main factor that limits the specific detectivity of a photodetector. The total noise current of our phototransistor was directly measured with a lock-in amplifier. As shown in Figure 3b, the measured noise current was dominated by the shot noise, and accordingly, the specific detectivity of a photodetector is given by[14]

$$D^* = \frac{(Af)^{1/2}}{(i_n / R)} \tag{2}$$

where A, f and i_n are the effective area of the device, the electrical bandwidth and the noise current, respectively. The detectivity, together with the photoresponsivity, of our hybrid phototransistor as a function of wavelength is plotted in Figure 3c. At an illumination light intensity of 10 mW cm^{-2}, the maximum D^* of 3.68×10^{14} Jones at about 400 nm was obtained from the hybrid device, whereas the phototransistor based on the pristine perovskite showed a much lower D^* of 4.0×10^{12} Jones (see Figure S11b). We note here that the obtained D^* is comparable to the highest values reported for perovskite-based photodetectors (a comparison with some typical works on perovskite-based photodetectors is given in Table S2),[14,16,18-20,26] making the hybrid phototransistor attractive for high-sensitivity optoelectronics.

To further examine the role of CNTs in hybrid films, we investigated a series of perovskite-based phototransistors comprising different concentrations of CNTs. As shown in Figure 3d, the highest mobility and the optimal device performance were obtained at a concentration of 1 wt.%. We should note that the hole mobility of nearly 600 cm^2 V^{-1} s^{-1} is the highest among the values reported for perovskite-based materials, including perovskite single crystals.[23-25] In our hybrid films, CNTs play an important role in interacting with the perovskite and transporting charges, thereby significantly improving the overall mobility. However, at a high concentration of CNTs (3 wt.%), the resulting device showed a high conductance but a weak p-type field effect (Figure S12). This suggested the formation of a percolation network of CNTs, which dominated the charge transport. Since photocurrent is proportional to mobility, the optimal photoresponsivity and detectivity of the phototransistors

were also achieved with 1 wt.% of CNTs (Figure 3d). Moreover, we measured 20 plus hybrid phototransistors with 1 wt.% of CNTs and the statistics of their performance were summarized in Figure S13. Such hybrid devices exhibited high sensitivity toward moisture, light and other factors in ambient conditions.
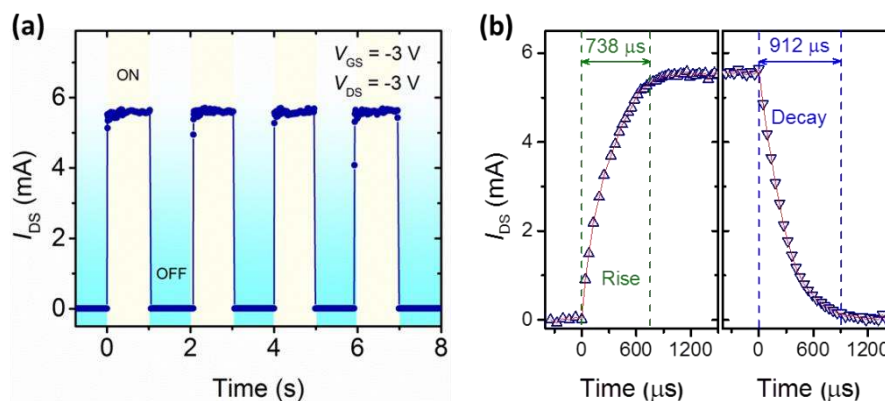

Figure 4. Photocurrent response of the hybrid perovskite/CNTs phototransistor. (a) Temporal Photocurrent responsive characteristic of the hybrid perovskite/CNTs phototransistor measured at V_{GS} = -3 V and V_{DS} = -3 V, respectively. (b) Temporal photocurrent response, indicating a rise time of 738 µs and a decay time of 912 µs.

Another important parameter of optoelectronic devices is their response speed. The temporal response of the hybrid phototransistor was characterized using chopper-generated light pulses with a time interval of 1.0 s and an intensity of 10 mW cm^{-2}. The device was measured under biases of V_{DS} = -3 V and V_{GS} = -3 V. As shown in **Figure 4a**, the dynamic photoresponse of the hybrid phototransistor is stable and reproducible, indicating that the device can function as a good light switch. The temporal photocurrent response of the hybrid phototransistor is presented in Figure 4b. The switching times for the rise (output signal changing from 0 to 90% of the peak output value) and the decay (I_{DS} decreasing from peak value to 10%) of the photocurrent are about 738 µs and 912 µs, respectively, which can also be taken as the carrier lifetime τ_{life}. It is noted that the response speed of our hybrid phototransistor is faster than most of organic, quantum dot and hybrid photodetectors (typically on the order of milliseconds),[18,27,28,31,48-50] which arise from good carrier transport

in the hybrid films. The photoconductive gain (G) is the ratio between τ_{life} and the transit time (τ_{tran}, which is the time during which holes sweep through the CNTs to the electrodes), and given by[16,27,29,31]

$$G = \frac{\tau_{life}}{\tau_{tran}} = \frac{\tau_{life}}{L^2 / \mu \cdot V_{DS}} \tag{3}$$

Based on the measured carrier recombination time and the carrier mobility, the gain of our hybrid devices was estimated to be approximately 8000, which further underscores the hybrid perovskite/CNT films as a promising material candidate for photoelectronic applications.

In summary, we have demonstrated a novel type of hybrid thin films by combining light-absorbing perovskite and carrier-transporting CNTs. In DMF solutions, halide perovskite and CNTs are found to possess excellent material compatibility and can be processed into high-quality composite films. Furthermore, detrimental Coulomb scatterings are effectively suppressed as a result of the type-II band alignment at the interfaces and the high quality of the perovskite/CNT composite films. The ambipolar phototransistors made from such perovskite/CNTs films exhibit excellent figures of merit, including an remarkable hole mobility of 595.3 cm^2 V^{-1} s^{-1}, an ultrahigh specific detectivity of 3.68×10^{14} Jones, and a fast response time of several hundred μs. From a general perspective, these perovskite/CNTs composite films open up a new door toward developing high-performance optoelectronic devices, and the strategy may help advance other hybrid-based technologies.

Experimental Section

Perovskite/CNTs solution preparation: Semiconducting CNTs with (7,6) chirality (Sigma-Aldrich, > 98 wt.%) were purified via refluxing in 3M HNO_3 for 12 h. Then, the CNTs were separated by ultracentrifugation, washed with excess of water several times and freeze-dried. Methylammonium iodide (MAI) and lead(II) chloride ($PbCl_2$, Sigma-Aldrich, 98%) were dissolved in DMF (Sigma-Aldrich, 99.8%) with a molar ratio 3:1 to form the perovskite precursor solution. To form the perovskite/CNTs solution, the purified CNTs was mixed into

the perovskite solution upon sonication for 2 h., with the CNTs/perovskite weight concentration ranging from 0 and 3%. The precursor solution must be stored in glove box and used quickly after mixing to avoid degradation.

Device fabrication: Si/SiO$_2$ (300 nm) substrates were cleaned by sonication in acetone, ethanol and deionized water, respectively. After drying in flowing nitrogen, we treated the substrates with oxygen plasma. The hybrid solution was spin-coated on substrates at 2000 rpm for 20 seconds and annealed at 100 °C for 60 minutes in a glove box. For comparison, pristine perovskite films were prepared without CNTs following the same protocol. Ti/Au (5 nm/80 nm) source (S) and drain (D) electrodes were deposited via thermal evaporation through a shadow mask, defining phototransistor channels with length of 50 μm and width of 1000 μm. Finally, the fabricated devices were annealed to reduce the charge traps and to improve the contacts between the active layer and the S/D electrodes.

Measurements: XRD was performed on a Bruker D8-Advance diffractometer using Cu Kα radiation (λ = 1.5406 Å). The surface morphology of the films was measured using SEM (FEI Nova Nano 630). TEM experiments were carried out using a Titan ST instrument operated at 300 kV. The absorption and steady-state PL were recorded using Cary 6000i spectrophotometer with an Edinburgh Instrument spectrofluorometer. Helios UV-NIR femtosecond transient absorption spectroscopy system (Ultrafast Systems, LLC) was used to characterize the samples. Transport measurements were conducted using a Signotone Micromanipulator S-1160 probe station equipped with LED and Keithley 4200 SCS. Noise current was measured with a lock-in amplifier SR830.

Supporting Information
Supporting Information is available from the Wiley Online Library or from the author.

[1]   G. Xing, N. Mathews, S. Sun, S. S. Lim, Y. M. Lam, M. Gratzel, S. Mhaisalkar, T. C. Sum, *Science* **2013**, 342, 344.

[2]   S. D. Stranks, G. E. Eperon, G. Grancini, C. Menelaou, M. J. P. Alcocer, T. Leijtens, L. M. Herz, A. Petrozza, H. J. Snaith, *Science* **2013**, 342, 341.

[3]   C. Wehrenfennig, G. E. Eperon, M. B. Johnston, H. J. Snaith, L. M. Herz, *Adv. Mater.* **2014**, 26, 1584.

[4]   O. Malinkiewicz, A. Yella, Y. H. Lee, G. M. Espallargas, M. Graetzel, M. K. Nazeeruddin, H. J. Bolink, *Nat. Photon.* **2014**, 8, 128.

[5]   S. D. Stranks, H. J. Snaith, *Nat. Nanotech.* **2015**, 10, 391.

[6]   J. Burschka, N. Pellet, S.-J. Moon, R. Humphry-Baker, P. Gao, M. K. Nazeeruddin, M. Grätzel, *Nature* **2013**, 499, 316.

[7]   J. H. Kim, P.-W. Liang, S. T. Williams, N. Cho, C.-C. Chueh, M. S. Glaz, D. S. Ginger, A. K.-Y. Jen, *Adv. Mater.* **2015**, 27, 695.

[8]   D. Bi, P. Gao, R. Scopelliti, E. Oveisi, J. Luo, M. Grätzel, A. Hagfeldt, M. K. Nazeeruddin, *Adv. Mater.* **2016**, 28, 2910.

[9]   F. Giordano, A. Abate, J. P. Correa Baena, M. Saliba, T. Matsui, S. H. Im, S. M. Zakeeruddin, M. K. Nazeeruddin, A. Hagfeldt, M. Graetzel, *Nat. Commun.* **2016**, 7, 10379.

[10]   Z.-K. Tan, R. S. Moghaddam, M. L. Lai, P. Docampo, R. Higler, F. Deschler, M. Price, A. Sadhanala, L. M. Pazos, D. Credgington, F. Hanusch, T. Bein, H. J. Snaith, R. H. Friend, *Nat. Nanotech.* **2014**, 9, 687.

[11]   Y.-H. Kim, H. Cho, J. H. Heo, T.-S. Kim, N. Myoung, C.-L. Lee, S. H. Im, T.-W. Lee, *Adv. Mater.* **2015**, 27, 1248.

[12]   X. Y. Chin, D. Cortecchia, J. Yin, A. Bruno, C. Soci, *Nat. Commun.* **2015**, 6, 7383.

[13]   W. Peng, L. Wang, B. Murali, K.-T. Ho, A. Bera, N. Cho, C.-F. Kang, V. M. Burlakov, J. Pan, L. Sinatra, C. Ma, W. Xu, D. Shi, E. Alarousu, A. Goriely, J.-H. He, O. F. Mohammed, T. Wu, O. M. Bakr, *Adv. Mater.* **2016**, 28, 3383-3390.

[14]   L. Dou, Y. Yang, J. You, Z. Hong, W.-H. Chang, G. Li, Y. Yang, *Nat. Commun.* **2014**, 5, 5404.

[15]   H. Zhu, Y. Fu, F. Meng, X. Wu, Z. Gong, Q. Ding, M. V. Gustafsson, M. T. Trinh, S. Jin, X.-Y. Zhu, *Nat. Mater.* **2015**, 14, 636.

[16] F. Li, C. Ma, H. Wang, W. Hu, W. Yu, A. D. Sheikh, T. Wu, *Nat. Commun.* **2015**, 6, 8238.

[17] G. Wang, D. Li, H.-C. Cheng, Y. Li, C.-Y. Chen, A. Yin, Z. Zhao, Z. Lin, H. Wu, Q. He, M. Ding, Y. Liu, Y. Huang, X. Duan, *Sci. Adv.* **2015**, 1, e1500613.

[18] Y. Lee, J. Kwon, E. Hwang, C. H. Ra, W. J. Yoo, J. H. Ahn, J. H. Park, J. H. Cho. *Adv. Mater.* **2015**, 27, 41.

[19] Y. Fang, J. Huang. *Adv. Mater.* **2015**, 27, 2804.

[20] M. I. Saidaminov, Md. A. Haque, M. Savoie, A. L. Abdelhady, N. Cho, I. Dursun, U. Buttner, E. Alarousu, T. Wu, O. M. Bakr, *Adv. Mater.* **2016**, 28, 8144–8149.

[21] Y. Shao, Z. Xiao, C. Bi, Y. Yuan, J. Huang, *Nat. Commun.* **2014**, 5, 5784.

[22] C. La-o-vorakiat, T. Salim, J. Kadro, M.-T. Khuc, R. Haselsberger, L. Cheng, H. Xia, G. G. Gurzadyan, H. Su, Y. M. Lam, R. A. Marcus, M.-E. Michel-Beyerle, E. E. M. Chia, *Nat. Commun.* **2015**, 6, 7903.

[23] D. Shi, V. Adinolfi, R. Comin, M. Yuan, E. Alarousu, A. Buin, Y. Chen, S. Hoogland, A. Rothenberger, K. Katsiev, Y. Losovyj, X. Zhang, P. A. Dowben, O. F. Mohammed, E. H. Sargent, O. M. Bakr, *Science* **2015**, 347, 519.

[24] Q. Dong, Y. Fang, Y. Shao, P. Mulligan, J. Qiu, L. Cao, J. Huang, *Science* **2015**, 347, 967-970.

[25] M. I. Saidaminov, A. L. Abdelhady, B. Murali, E. Alarousu, V. M. Burlakov, W. Peng, I. Dursun, L. Wang, Y. He, G. Maculan, A. Goriely, T. Wu, O. F. Mohammed, O. M. Bakr, *Nat. Commun.* **2015**, 6, 7586.

[26] C. Ma, Y. Shi, W. Hu, M.-H. Chiu, Z. Liu, A. Bera, F. Li, H. Wang, L.-J. Li, T. Wu, *Adv. Mater.* **2016**, 28, 3683–3689.

[27] G. Konstantatos, M. Badioli, L. Gaudreau, J. Osmond, M. Bernechea, F. Pelayo Garcia de Arquer, F. Gatti, F. H. L. Koppens, *Nat. Nanotech.* **2012**, 7, 363.

[28] K. Roy, M. Padmanabhan, S. Goswami, T. P. Sai, G. Ramalingam, S. Raghavan, A. Ghosh, *Nat. Nanotech.* **2013**, 8, 826-830.

[29] F. H. L. Koppens, T. Mueller, Ph. Avouris, A. C. Ferrari, M. S. Vitiello, M. Polini, *Nat. Nanotech.* **2014**, 9, 780.

[30] Z. Chen, J. W. F. To, C. Wang, Z. Lu, N. Liu, A. Chortos, L. Pan, F. Wei, Y. Cui, Z. Bao, *Adv. Energy Mater.* **2014**, 4, 1400207.

[31] S. Park, S. J. Kim, J. H. Nam, G. Pitner, T. H. Lee, A. L. Ayzner, H. Wang, S. W. Fong, M. Vosgueritchian, Y. J. Park, M. L. Brongersma, Z. Bao, *Adv. Mater.* **2015**, 27, 759.

[32]   D. Kufer, I. Nikitskiy, T. Lasanta, G. Navickaite, F. H. L. Koppens, G. Konstantatos, *Adv. Mater*. **2015**, 27, 176.

[33]   T. W. Odom, J.-L. Huang, P. Kim, C. M. Lieber, *Nature* **1998**, 391, 62.

[34]   M. F. Yu, B. S. Files, S. Arepalli, R. S. Ruoff, *Phys. Rev. Lett.* **2000**, 84, 5552.

[35]   X. Zhou, J.-K. Park, S. Huang, J. Liu, P. L. McEuen, *Phys. Rev. Lett.* **2005**, 95, 146805.

[36]   P. Avouris, M. Freitag, V. Perebeinos, *Nat. Photon.* **2008**, 2, 341.

[37]   Z. Liu, K. Zheng, L. Hu, J. Liu, C. Qiu, H. Zhou, H. Huang, H. Yang, M. Li, C. Gu, S. Xie, L. Qiao, L. Sun, *Adv. Mater.* **2010**, 22, 999.

[38]   R. Bandyopadhyaya, E. Nativ-Roth, O. Regev, R. Yerushalmi-Rozen, *Nano Lett.* **2002**, 2, 25.

[39]   P. Schulz, A.-W. Dowgiallo, M. Yang, K. Zhu, J. L. Blackburn, J .J. Berry, *J. Phys. Chem. Lett.* **2016**, 7, 418.

[40]   S. N. Habisreutinger, T. Leijtens, G. E. Eperon, S. D. Stranks, R. J. Nicholas, H. J. Snaith, *Nano Lett.* **2014**, 14, 5561−5568.

[41]   J.-M. Liu, Photonic Devices (Cambridge University Press, Cambridge, UK **2009**).

[42]   O. F. Mohammed, D. Xiao, V. S. Batista, E. T. J. Nibbering, *J. Phys. Chem. A* **2014**, 118, 3090.

[43]   M. B. Price, J. Butkus, T. C. Jellicoe, A. Sadhanala, A. Briane, J. E. Halpert, K. Broch, J. M. Hodgkiss, R. H. Friend, F. Deschler, *Nat. Commun.* **2015**, 6, 8420.

[44]   D. K. Schroder, Semiconductor Material and Device Characterization (Wiley, **2006**).

[45]   N. B. Prince, *II. Silicon. Phys. Rev.* **1954**, 93, 1204.

[46]   P. Y. Yu, M. Cardona, *Fundamentals of Semiconductors: Physics and Materials Properties*, 4th ed. (Springer, Berlin, 2010).

[47]   G. Konstantatos, E. H. Sargent, *Nat. Nanotech.* **2010**, 5, 391–400.

[48]   K.-J. Baeg, M. Binda, D. Natali, M. Caironi, Y.-Y. Noh, *Adv. Mater.* **2013**, 25, 4267–4295.

[49]   M. Saidaminov, V. Adinolfi, R. Comin, A. L. Abdelhady, W. Peng, I. Dursun, M. Yuan, S. Hoogland, E. H. Sargent, O. M. Bakr, *Nat. Commun.* **2015**, 6, 8724.

[50]   G. Konstantatos, I. Howard, A. Fischer, S. Hoogland, J. Clifford, E. Klem, L. Levina, E. H. Sargent, *Nature* **2006**, 442, 180–183.

A simple and straightforward synthetic strategy to enhance the carrier mobility of photo-responsive hybrid perovskite films is realized via coupling with single-walled carbon nanotubes. Hole and electron mobilities of the composite films reach record-high values of 595.3 and 108.7 cm^2 V^{-1} s^{-1}, respectively, and ambipolar phototransistors exhibit an ultrahigh detectivity of 3.7×10^{14} Jones and a responsivity of 1×10^4 A W^{-1}. Such perovskite/carbon nanotube composite films provide a versatile platform for diverse fields of optoelectronics, solar energy conversion, and molecular sensing.

Keywords: photodetector, phototransistor, perovskite, carbon nanotubes, mobility

Feng Li, Hong Wang, Dominik Kufer, Liangliang Liang, Weili Yu, Erkki Alarousu, Chun Ma, Yangyang Li, Zhixiong Liu, Changxu Liu, Nini Wei, Fei Wang, Lang Chen, Omar F. Mohammed, Andrea Fratalocchi, Xiaogang Liu, Gerasimos Konstantatos, and *Tom Wu**

Ultrahigh Carrier Mobility Achieved in Photo-responsive Hybrid Perovskite Films via Coupling with Single-Walled Carbon Nanotubes

ToC figure
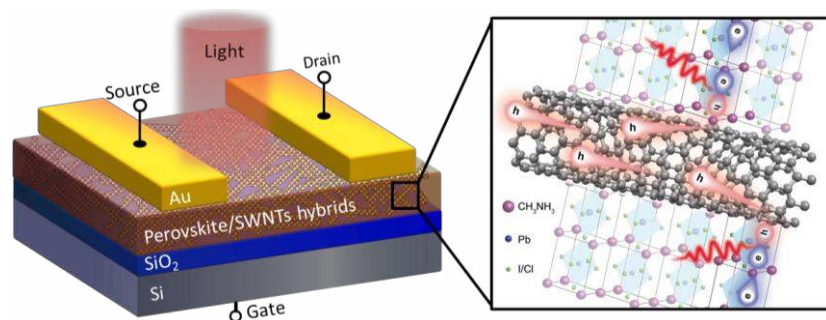
Supporting Information

Ultrahigh Carrier Mobility Achieved in Photo-responsive Hybrid Perovskite Films via Coupling with Single-Walled Carbon Nanotubes

Feng Li, Hong Wang, Dominik Kufer, Liangliang Liang, Weili Yu, Erkki Alarousu, Chun Ma, Yangyang Li, Zhixiong Liu, Changxu Liu, Nini Wei, Fei Wang, Lang Chen, Omar F. Mohammed, Andrea Fratalocchi, Xiaogang Liu, Gerasimos Konstantatos, and Tom Wu*
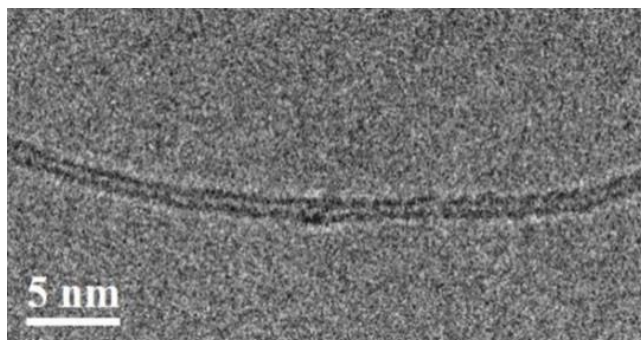
*E-mail: tao.wu@kaust.edu.sa

Figure S1. High-resolution transmission electron microscopy (HRTEM) image of a SWNT used to fabricate the perovskite/SWNTs hybrids. The diameter of SWNT is about 1.4 nm.

19
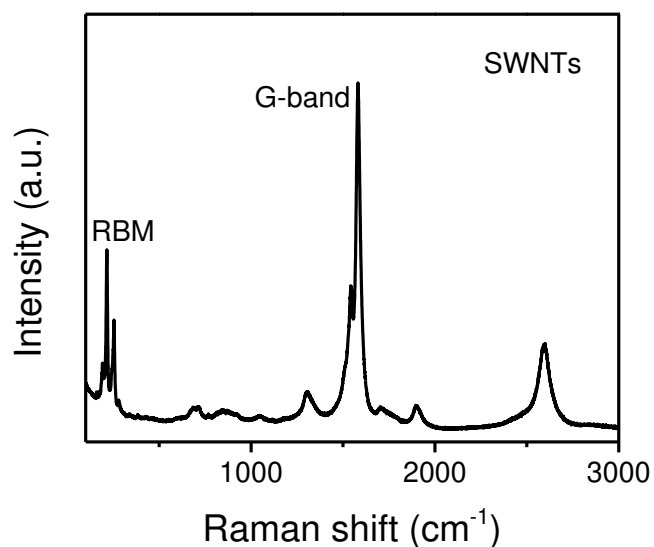
Figure S2. Raman spectrum of SWNTs used to fabricate perovskite/SWNTs hybrids.

Figure S3. Digital photographs of (I) the $CH_3NH_3PbI_{3-x}Cl_x$/SWNTs precursor and (II) SWNTs in N, N-dimethylformamide (DMF) solutions taken 24 h after preparation. A homogeneous, dark dispersion of SWNTs in DMF solution of CH_3NH_3I and $PbCl_2$ was prepared, and remarkably, it remained stable for more than 24 h without precipitation, while the pristine SWNTs quickly precipitated out in DMF solution.
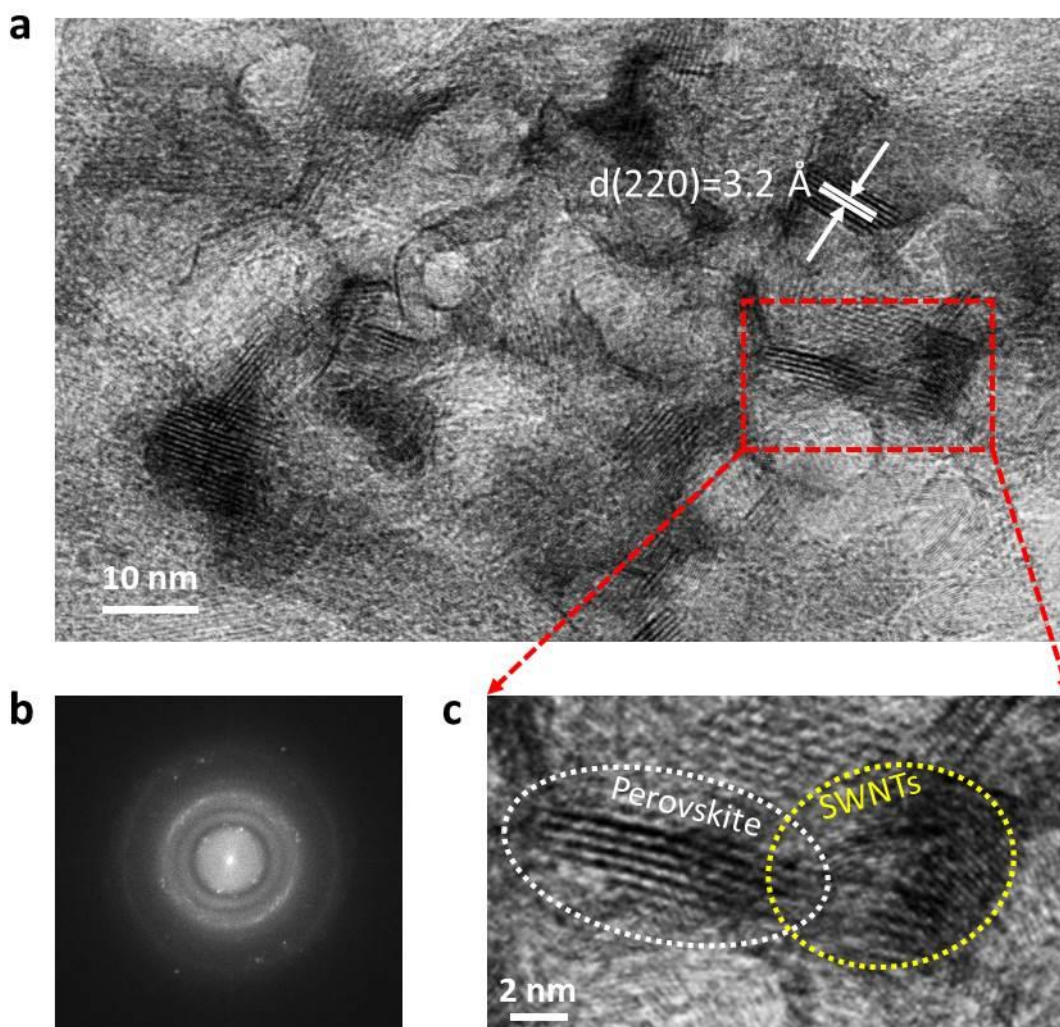
Figure S4. TEM data of the hybrid film. (a) Transmission electron microscopy (TEM) image of the hybrid perovskite/CNTs film. Note that the contrast of the curling CNTs is much weaker than that of perovskite due to their lower molecular weight. (b) Selected area electron diffraction (SAED) pattern. Symmetric diffraction spots and continuous diffraction rings displayed in the SAED pattern belong to crystalline perovskite and CNTs, respectively. (c) Closer view of an area with perovskite and CNTs in proximity to each other, forming close interfaces.
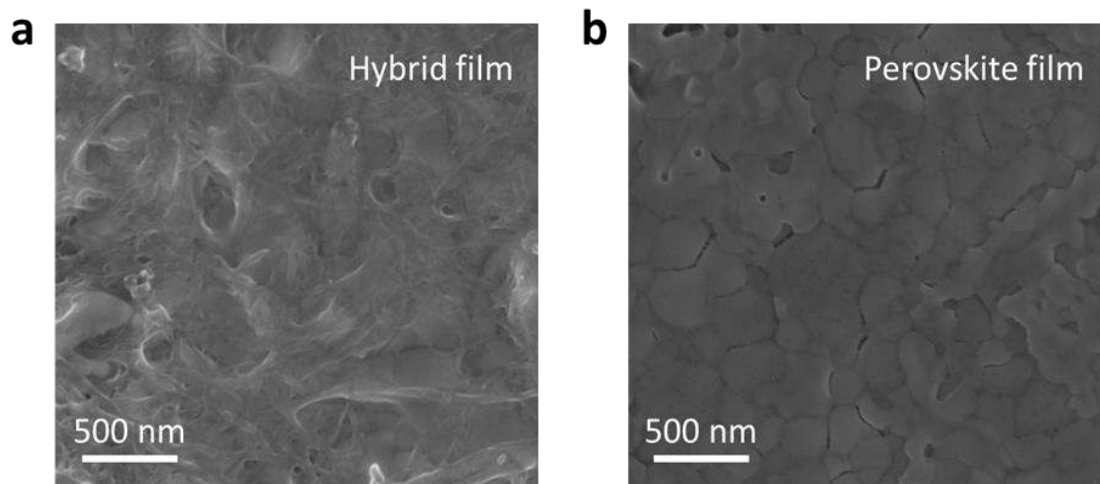
Figure S5. SEM images of the films. (a) Scanning electron microscopy (SEM) image of the perovskite/SWNTs film on Si/SiO$_2$ substrate. The hybrid thin film appears smooth and uniform surface morphology. Some SWNTs replace perovskites in the hybrid thin film, and the superior tracks are used to achieve carrier transport with less scatter. (b) SEM image of a pristine perovskite film on Si/SiO$_2$ substrate. The pristine perovskite film suffers from poor surface coverage and pinholes.
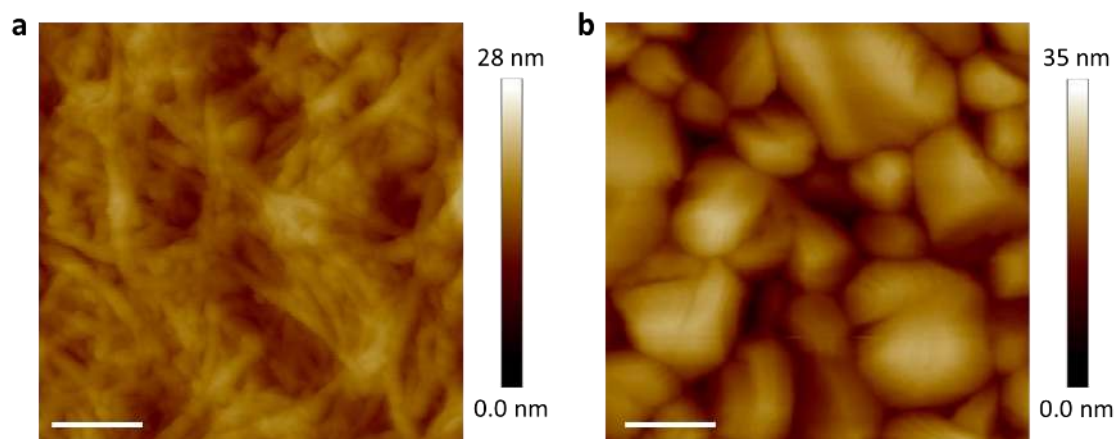
Figure S6. Atomic force microscopy (AFM) characterizations of the hybrid and perovskite films. The root-mean square roughness of the hybrid film is approximately 7.83 nm, demonstrating a smoother surface compared to that of the perovskite film. Scale bar, 500 mm.
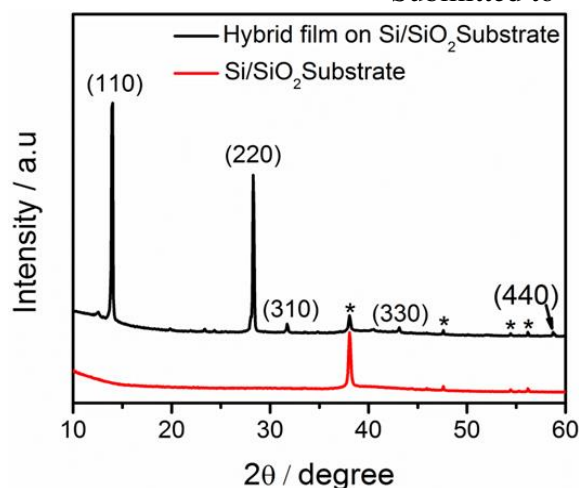
Figure S7. XRD pattern of the films. X-ray diffraction (XRD) spectra of the hybrid perovskite/SWNTs film on Si/SiO$_2$ substrate (black line) and the sole Si/SiO$_2$ substrate (red line), respectively. The peaks marked with * belong to the Si/SiO$_2$ substrate. The main diffraction peaks at 14.02°, 28.35°, 37.74°, 43.16° and 58.78° can be assigned to <110>, <220>, <310>, <330>, <440> planes of the perovskite, respectively, which the perovskite CH$_3$NH$_3$PbI$_{3-x}$Cl$_x$ composited to hybrid thin film possess the expected orthorhombic crystal structure with high crystallinity.
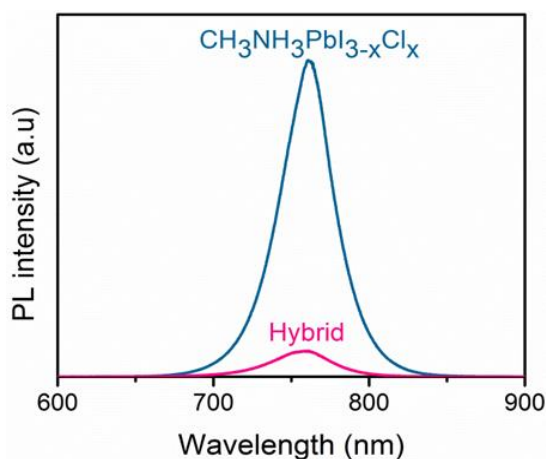

Figure S8. PL spectra. Steady-state photoluminescence (PL) spectra of the hybrid perovskite/SWNTs and the pristine perovskite films. A strong quenching of the perovskite PL peak at ~760 nm was observed upon the addition of SWNTs.
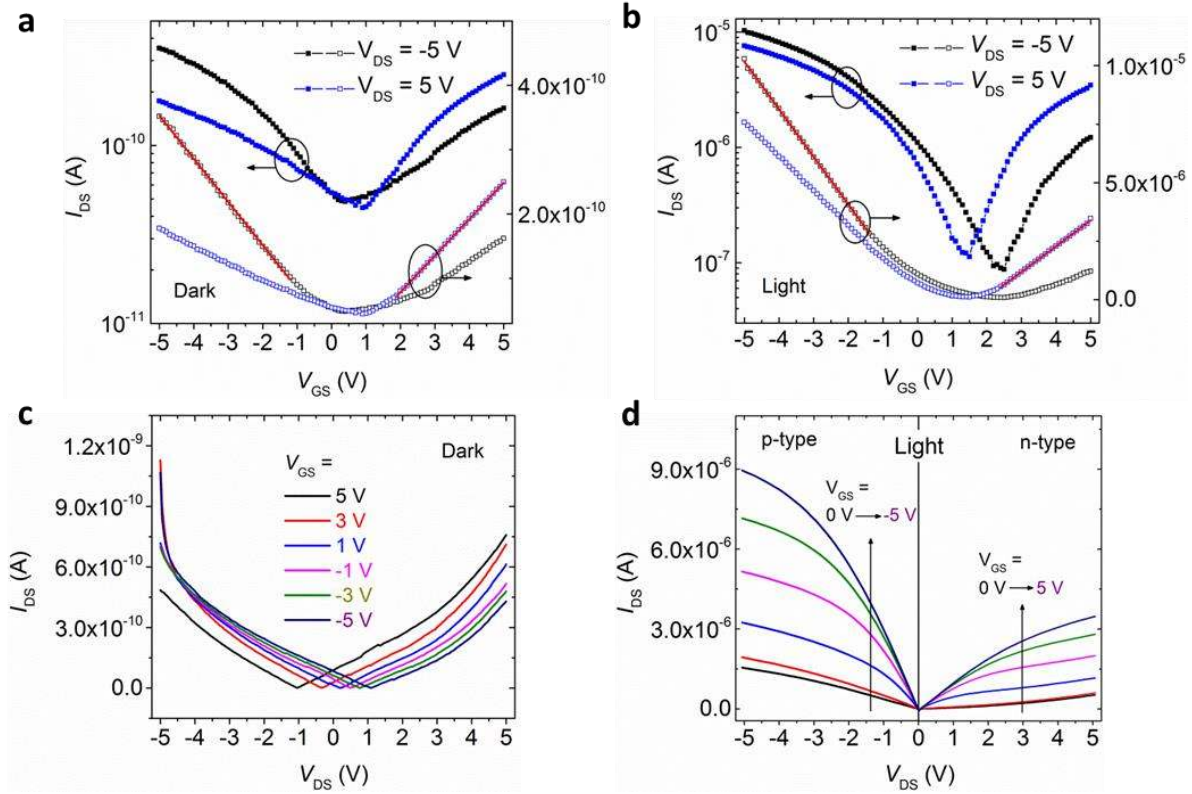
Figure S9. Performance of a control device employed the pure perovskites in the phototransistor channel. (a,b) Transfer characteristics of the perovskite-based phototransistor in the dark and under light illumination, respectively. The field-effect hole/electron mobilites, calculated from the transconductance using $I_{DS} = \dfrac{W}{L}C_i\mu(V_{GS} - V_{TH})V_{DS}$ in the linear regime, are just $1.62 \times 10^{-4}/1.17 \times 10^{-4}$ cm^2 V^{-1} s^{-1} in the dark condition and $1.37/0.87$ cm^2 V^{-1} s^{-1} under light illumination, respectively. (c,d) Output characteristic of the perovskite phototransistor in dark and under light illumination, respectively.
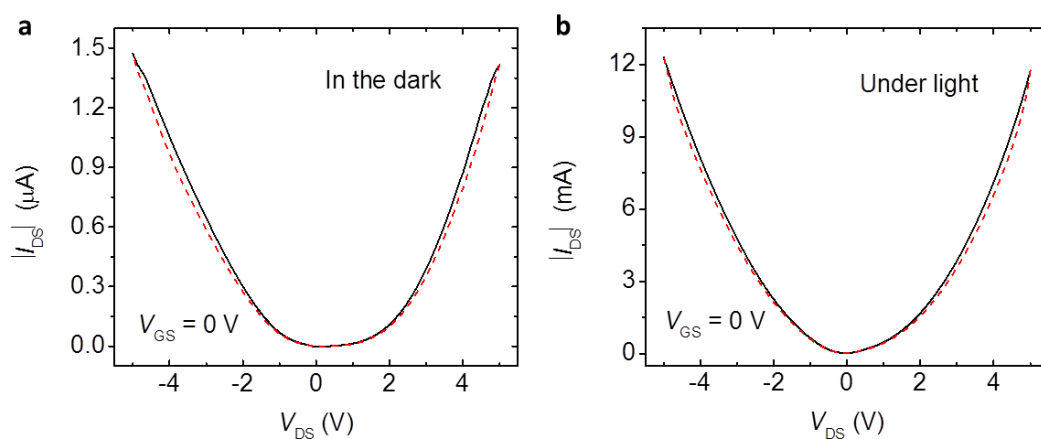
Figure S10. *I-V* curves for the device without the gate bias. The dependence of I_{DS} on V_{DS} for the hybrid phototransistor at $V_{GS} = 0$ V, measured in the dark and under light illumination, showing symmetric behavior without any current rectification.
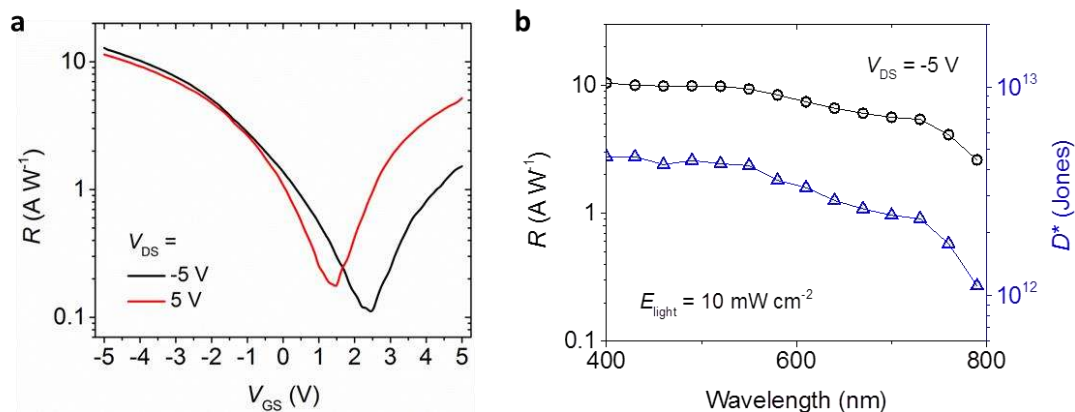
Figure S11. Performance of the perovskite phototransistor. (a) Responsivity (R) of the perovskite-based phototransistor operating at V_{DS} = -5 V and V_{DS} = 5 V, respectively. (b) Responsivity (R) and specific detectivity (D^*) of the perovskite phototransistor at different wavelengths with the light intensity of 10 mW cm^{-2}.
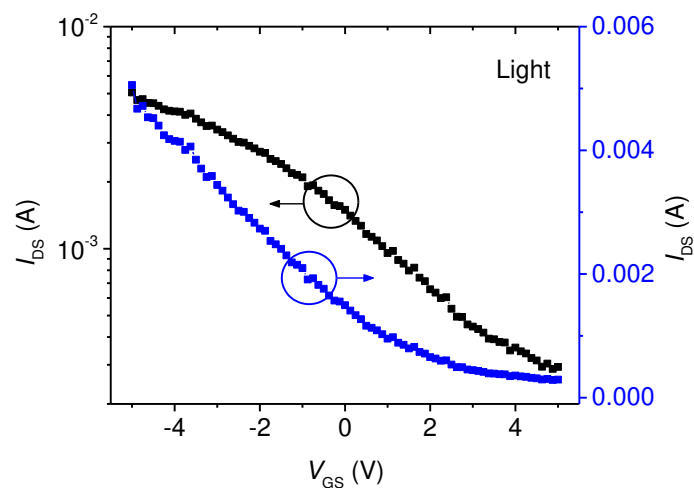

Figure S12. Transfer characteristics of a hybrid phototransistor with the SWNTs concentration of 3 wt. %. The hybrid film presents high conductance but a weak p-type field effect, indicating that the SWNTs form a fully percolation network, which dominates the charge transport.
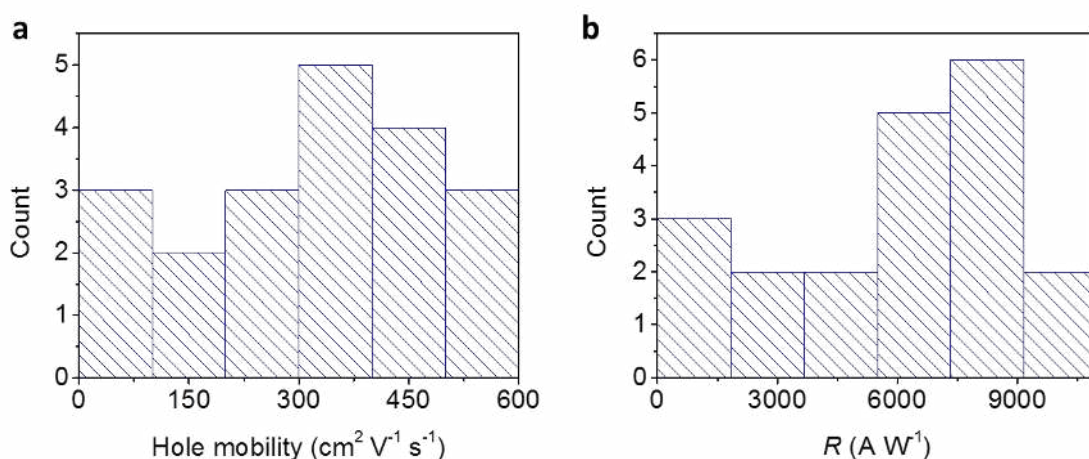
Figure S13. Performance statistics of the hybrid phototransistors. Histograms of the performance (a, hole mobility values; b, responsivity values) measured on 20 devices using the perovskite/SWNTs hybrid film with the SWNTs concentration of 1 wt. %. We observed notable fluctuations of hole mobility (μ_h) and responsivity (R), which appears to correlate with the high sensitivity of devices toward moisture, room light and other factors in ambient conditions. Therefore, further experiments are warranted to explore the optimal and reproducible fabrication of hybrid phototransistors with embedded SWNTs in halide perovskite films.

Table S1. A summary of published typical carrier mobility of hybrid perovskites.

Ref.	Year	Material	Carrier mobility (cm^2 V^{-1} s^{-1})	Condition	Mothed
1	2013	$CH_3NH_3PbI_3$ film	~66	RT[a]	Hall-effect measurements
2	2014	$CH_3NH_3PbI_{3-x}Cl_x$ film	11.6	RT	transient THz spectroscopy
3	2014	$CH_3NH_3PbI_3$ film	25	RT	Combination of PL[b], TA[c], TRTS[d], and TRMC[e] measurements
4	2015	$CH_3NH_3PbI_3$ film	7.2×10^{-2}	78 K	Light-emitting field-effect transistor
5	2015	$CH_3NH_3PbI_{3-x}Cl_x$ film	1.24	RT, Under illumination	Phototransistors
6	2015	$CH_3NH_3PbI_{3-x}Cl_x$ film	1.3	RT	Field-effect transistors
7	2015	$CH_3NH_3PbI_3$ film	$\sim 7.5 \times 10^{-3}$	150 K	Field-effect transistors
8	2015	$CH_3NH_3PbI_3$ single crystal	2.5	300 K	SCLC[f] technique
8	2015	$CH_3NH_3PbBr_3$ single crystal	115	300 K	Time-of-flight technique
9	2015	$CH_3NH_3PbI_3$ single crystal	164 ± 25	RT	SCLC technique
10	2015	$CH_3NH_3PbI_3$ single crystal	67.2 ± 7.3	RT	SCLC technique
10	2015	$CH_3NH_3PbBr_3$ single crystal	24.0 ± 0.3	RT	SCLC technique
11	2015	$CH_3NH_3PbI_3$ microplate crystal	~2.5	77 K	Field-effect transistors
12	2015	$CH_3NH_3PbCl_3$ single crystal	42 ± 9	RT	SCLC technique

[a]RT: room temperature. [b]PL: photoluminescence. [c]TA: transient absorption. [d]TRTS: time-resolved terahertz spectroscopy. [e]TRMC: time-resolved microwave conductivity. [f]SCLC: space-charge-limited current.

Table S2. Progress in the performance of the photodetectors based on hybrid perovskites.

Ref.	Year	Materials	Configuration	Responsivity (A W^{-1})	Detectivity (Jones)	Response time
13	2014	$CH_3NH_3PbI_3$ film	solar cell	The photocurrent amplification (over 100)		
14	2014	$CH_3NH_3PbI_3$/TiO_2 film	photodetector	0.49×10^{-6}		0.02 s
15	2014	$CH_3NH_3PbI_3$ film	photodetector	3.49		< 0.2 s
16	2014	$CH_3NH_3PbI_{3-x}Cl_x$ film	photodetector		$\sim 10^{14}$	160 ns
17	2014	$CH_3NH_3PbI_3$ nanowires	phototransistor	5×10^{-3}		< 500 μs
18	2015	$CH_3NH_3PbI_3$ film	phototransistor	14.5		0.2 μs
19	2015	Graphene-$CH_3NH_3PbI_3$ composites	phototransistor	180	$\sim 10^{9}$	87 ms
20	2015	$CH_3NH_3PbI_3$ film	photodetector	242		5.7 ± 1.0 μs
21	2015	$CH_3NH_3PbI_3$ film	photodiode		3×10^{12}	< 5 μs
22	2015	$CH_3NH_3PbI_3$ film	photodetector		7.4×10^{12}	120 ns
23	2015	$CH_3NH_3PbI_3$ film	optocoupler	1.0		20 μs
24	2015	$CH_3NH_3PbI_3$ nanowires	photodetector	1.3	2.5×10^{12}	0.3 ms
5	2015	$CH_3NH_3PbI_3$/$CH_3NH_3PbI_{3-x}Cl_x$ film	phototransistor	320/47		5 μs
25	2015	$CH_3NH_3PbI_3$ /nanocrystalline graphite film	photodetector	0.795		< 25 ms
26	2016	$CH_3NH_3PbI_3$/MoS_2 hybrid structure	photodetector	1.94×10^{6}	1.29×10^{12}	6.2 s
27	2016	Heterostructured WS_2/$CH_3NH_3PbI_3$	photoconductor	17	2×10^{12}	2.7 ms
10	2016	planar-integrated $CH_3NH_3PbBr_3$ single-crystal	photodetector	4000		25 μs

References

[1]   C. C. Stoumpos, *et al. Inorg. Chem.* **2013**, 52, 9019.

[2]   C. Wehrenfennig, *et al. Adv. Mater.* **2014**, 26, 1584.

[3]   C. S. Ponseca, *et al. J. Am. Chem. Soc.* **2014**, 136, 5189.

[4]   X. Y. Chin, *et al. Nature Commun.* **2015**, 6, 7383.

[5]   F. Li, *et al. Nature Commun.* **2015**, 6, 8238.

[6]   Y. Mei, *et al. MRS Commun.* **2015**, 5, 297.

[7]   J. G. Labram, *et al. J. Phys. Chem. Lett.* **2015**, 6, 3565.

[8]   D. Shi, D. *et al. Science* **2015**, 347, 519.

[9]   Q. F. Dong, *et al. Science* **2015**, 347, 967–970.

[10]   M. I. Saidaminov, *et al. Nature Commun.* **2015**, 6, 7586.

[11]   G. Wang, *et al. Sci. Adv.* **2015**, 1, e1500613.

[12]   G. Maculan, *et al. J. Phys. Chem. Lett.* **2015**, 6, 3781−3786.

[13]   T. Moehl, *et al. J. Phys. Chem. Lett.* **2014**, 5, 3931-3936.

[14]   H.-R. Xia, *et al. Chem. Commun.* **2014**, 50, 13695–13697.

[15]   X. Hu, *et al. Adv. Funct. Mater.* **2014**, 24, 7373–7380.

[16]   L. Dou, *et al. Nat. Commun.* **2014**, 5, 5404.

[17]   E. Horváth, *et al. Nano Lett.* **2014**, 14, 6761−6766.

[18]   Y. Guo, *et al. J. Phys. Chem. Lett.* **2015**, 6, 535−539.

[19]   Y. Lee, *et al. Adv. Mater.* **2015**, 27, 41–46.

[20]   R. Dong, *et al. Adv. Mater.* **2015**, 27, 1912–1918.

[21]   Q. Lin, *et al. Adv. Mater.* **2015**, 27, 2060–2064.

[22]   Y. Fang, *et al. Adv. Mater.* **2015**. DOI: 10.1002/adma.201500099.

[23]   D. Li, *et al. Sci. Rep.* **2015**, 5, 7902.

[24]   H. Deng, *et al. Nanoscale* **2015**, 7, 4163.

[25]   Y. Wang, *et al. Nanotechnology* **2016**, 27, 175201.

[26]   D.-H. Kang, *et al. Adv. Mater.* **2016**. DOI: 10.1002/adma.201600992.

[27]   C. Ma, *et al. Adv. Mater.* **2016**, 28, 3683–3689.